Supporting Information

Unveiling the genesis of the high catalytic activity in nickel phthalocyanine for electrochemical ammonia synthesis

Shyamal Murmu[1], Sourav Paul[1], Samadhan Kapse[2], Ranjit Thapa[2], Santanu Chattopadhyay[3], Abharana N[4], Shambhu N. Jha[4], Dibyendu Bhattacharyya[4] and Uttam Kumar Ghorai[1]*

[1]Department of Industrial Chemistry & Applied Chemistry, Swami Vivekananda Research Centre, Ramakrishna Mission Vidyamandira, Belur Math, Howrah – 711202, India
[2]Department of Physics, SRM University – AP, Amaravati 522240, Andhra Pradesh, India
[3]Rubber Technology Centre, Indian Institute of Technology, Kharagpur – 721302, India
[4]Atomic & Molecular Physics Division, Bhabha Atomic Research Centre, Mumbai – 400085, India

Corresponding author:
***Email:** uttam.indchem@vidyamandira.ac.in

Contents

SI 12: XPS high resolution spectrum of Ni 2p doublet

SI 13: High resolution XPS spectrum of N 1s

SI 14: FTIR spectrum of NiPc NRs

SI 15: UV-vis spectrum of NiPc NRs

SI 16: FTIR spectrum of commercial NiPc

SI 17: UV-vis spectrum of commercial NiPc

SI 18: Experimental XANES spectra of NiPc samples measured at Ni K-edge

SI 19: Schematic representation of H-type electrochemical setup

SI 20: LSV profile of NiPc NRs in Ar & N_2 saturated 0.1 M HCl solution

SI 21: UV-vis absorption spectra given concentration of NH_4^+ solution

SI 22: Calibration curve used for calculating the NH_4^+ concentration

SI 23: UV-vis absorption spectra of different N_2H_4 concentration

SI 24: Calibration curve used for determination of N_2H_4 concentration

SI 25: UV-vis absorption spectra for the formation of N_2H_4

SI 26: ^{1}H NMR spectra of $(^{14}NH_4)_2SO_4$ with varying concentration

SI 27: Calibration plot for the determination of $^{14}NH_4^+$ concentration by NMR method

SI 28: Comparative bar diagram of average NH_3 yield rate by ^{1}H NMR and UV-vis method

SI 29: UV-vis absorption of NiPc NRs sample at –0.3 V *vs.* RHE in Ar saturated, N_2 saturated open circuit potential and blank GCE

SI 30: UV-vis absorption of NiPc NRs at –0.3 V *vs.* RHE for different cycles

SI 31: Durability test at different time interval(s) for NiPc NRs towards NRR at –0.3 V *vs.* RHE in N_2 saturated electrolyte

SI 32: UV-vis absorption of NiPc NRs at –0.3 V *vs.* RHE for long term stability test

SI 33: XPS survey spectrum of NiPc NRs after NRR

SI 34: HRTEM image of NiPc NRs after stability test

SI 35: UV-vis absorption spectra of NO_x of various concentration solutions

SI 36: Calibration curve of NO_x with the various concentrations

SI 37: UV-vis spectra of electrolytes saturated with $^{14}N_2$ gas for detecting NO_x

SI 38: UV-vis absorption spectra of the electrolytes stained with an indophenol indicator at different potential for Pc

SI 39: Histogram of average NH_3 yield rate and corresponding FE of Pc at different potential

SI 40: Comparison of NH_3 yield rate and FE of NiPc NRs and Pc at –0.3 V *vs*. RHE

SI 41: Table S1: Comparison of the NRR activity for NiPc NRs with other transition metal based electrocatalyst in solution media of varying pH

SI 42: References

SI 1: EXAFS measurements

EXAFS measurements on nickel pthalocyanine before and after electrolysis samples were examined at energy scanning EXAFS beamline (BL-09) at Indus-2 Synchrotron source (2.5 GeV, 300 mA) at the Raja Ramanna Centre for Advanced Technology (RRCAT), Indore, India [1-2], where beam line functions in the photon energy range of 4-25 KeV. The beamline optics comprises of Rh/Pt coated collimating meridional cylindrical mirror used to collimate the beam. This mirror is utilized prior to DCM for the rejection of higher harmonies to certain extent. The collimated beam undergoes monochromatization by a Si (111) ($2d = 6.2709\,\mathring{A}$) based on double crystal monochromator (DCM). The second crystal of DCM is a sagittal cylindrical crystal, which is utilized for horizontal focusing of beam while other Rh/Pt coated bendable post mirror faced downwards is applied for vertical focus of beam at sample position.

In the event of samples, the information has been recorded at Ni K-edges in the fluorescent mode. For present sample, the measurement is done in the fluorescent mode utilizing a Si drift detector (Vortex detector) in 45deg geometry. Rejection of higher harmonic substance in X-ray beam was guided by detuning the second crystal of DCM. The coefficient of absorption μ is found by the relation:

$$I_T = I_0 e^{-\mu x} \qquad (1)$$

where, x denotes thickness of absorber and spectrum was acquired as a energy function of scanning the monochromator over defined range. The rejection of higher harmonic content in X-ray was also performed by detuning of the second crystal of DCM using the piezo motor to an extent such that the beam flux at the outlet of DCM is decreased to less than 30% of flux at its inlet.

To take heed of oscillations in absorption spectra $\mu(E)$ has been converted to the absorption function $\chi(E)$ mentioned as follows [3]:

$$\chi(E) = \frac{\mu(E) - \mu_0(E)}{\Delta\mu_0(E_0)} \qquad (2)$$

where, E_0 is absorption edge energy, $\mu_0(E_0)$ is bare atom background and $\Delta\mu_0(E_0)$ is step in $\mu(E)$ value at the absorption edge. The energy dependent absorption coefficient $\chi(E)$ has been changed to wave number dependent absorption coefficient $\chi(k)$ using the following relation,

$$K = \sqrt{\frac{2m(E - E_0)}{\hbar^2}} \qquad (3)$$

where, m is the electron mass. $\chi(k)$ is weighted by k^2 to amplify the oscillation at high k and the $\chi(k)k^2$ functions are fourier transformed in R space to generate $\chi(R)$ *vs.* R plots to the extent of real distances from center of an absorbing atom. A cluster of EXAFS data analysis tool available with Demeter software package have been purposefully used for EXAFS data analysis [4]. The procedure is inclusive of background reduction just as Fourier transform to get the $\chi(R)$ *vs.* R plots from absorption spectra (ATHENA software), the age of theoretical EXAFS spectra beginning from the supposed crystallographic structure (utilizing ATOMS subroutine).

SI 2: Determination of ammonia (NH_3)

The UV-visible spectroscopic technique of indophenol blue methodology was used to estimate the measure of ammonia produced during ENRR process. Experimentally, 2 ml of coloring solution (1 molar sodium hydroxide solution containing 5 wt% salicylic acid solution and 5 wt% trisodium citrate dihydrate (Merck Co., Ltd.)*) solution, 1 ml of oxidant (0.05 molar sodium hypochlorite solution (Merck Co., Ltd.)) and 0.2 ml of catalyst (3.34 milimolar solution of sodium nitroprusside dihydrate (Loba Chemie Co., Ltd)) were added to 2 ml solution taken from the electrochemical cell after NRR. The mixture solution was incubated at normal room temperature for two hours, and then spectroscopic estimations were completed. The UV-vis spectra showed maximum absorbance at 655 nm, implying the creation of indophenol blue.

For calibration, ammonium chloride (Merck Co., Ltd.) solution of different concentration {1.1, 0.9, 0.7, 0.5, 0.3, 0.1, 0.0 (μg/mL)} ammonium ions in 0.1M HCl solution then plot showing the different concentration with related to absorbance were measured. From the Figure S16, the fitting curve ($y = 0.221\ x + 0.014$; $R^2 = 0.999$) showed a linear relationship between absorbance and concentration, the outcome was consistent after three repeat experiments were done.

SI 3: Determination of hydrazine (N_2H_4)

The Watt and Chrisp method [5] were utilized to quantify the hydrazine produced during ENRR process. Specifically, colored solution was prepared in 300 ml of absolute ethanol (Merck Co. Ltd.), 30 ml HCl (concentrated) (Merck Co. Ltd.) and to it 5.99 g of para(dimethylamino) benzaldehyde (Merck Co. Ltd.) were added. Then 5 ml solution from electrochemical cell after ENRR experiment was taken and added with 5 ml of colored solution, then after incubation for 10 mins, in a dark at ambient temperature, and finally, the absorbance spectrum of the solution were taken which showed maximum absorbance at 455 nm. The calibration series were set up by following means: At first, a series of varying concentration of hydrazine-monohydrate as standard solutions (0.0, 0.1, 0.3, 0.5, 0.7, 0.9, 1.1 μg/mL) were made in 0.1 M HCl, then the volume was adjusted to 5 ml using 0.1 M HCl. Then 5 ml prepared hydrazine-hydrate solution was added in 5 ml colored solution, and stirring at normal temperature for a minute, further, the mixture of solution was incubated in dark for 10 minutes at normal temperature; then UV-visible spectroscopy were done and the maximum absorbance was noticed at 455 nm. The plot of concentration and absorbance curves (Figure S18) yielded a fitting plot ($y = 1.481x + 0.074$; $R^2 = 0.999$) which demonstrated a linear relationship between concentration of hydrazine-monohydrate and absorbance, after three independent experiments were completed then the amount of hydrazine formed were calculated.

SI 4: Isotope labelling experiments and quantification by ^{1}H NMR method

The isotope labelling experiment was performed using $^{15}N_2$ (98 atom% ^{15}N Sigma-Aldrich Co.) as the feeding gas to validate the source of ammonia formation. After $^{15}N_2$ gas was purged then electrolytic reaction was carried out at –0.3V (*vs*. RHE) for 6000 seconds, the formed $^{15}NH_4^+$ was determined by ^{1}H nuclear magnetic resonance (Bruker 400 MHz, USA). Similarly, the

quantitative determination of $^{14}NH_4^+$ was done using $^{14}N_2$ (99.999% ultra-high grade purity) as the feed gas, for calibration purpose $^{14}(NH_4)_2SO_4$ was used as standard.

SI 5: Quantitative determination of ammonia

The rate of formation of ammonia (R_{NH3}) was quantified using the following equation:

$$R_{NH_3} = \frac{\left(C_{NH_3} \text{ x } V\right)}{\left(t \text{ x } m\right)} \qquad (4)$$

Where 'C_{NH3}' is concentration of ammonia produced, 'V' is volume of the electrolyte, 't' is reaction time and 'm' is mass of the loaded catalyst.

The Faradaic efficiency (FE %) for ENRR was characterized as ratio of net charge required to produce ammonia by electrochemical means the net charge went through the electrode during electrochemical reaction

$$FE\ (\%) = \frac{\left(3 \text{ x } F \text{ x } C_{NH_3} \text{ x } V\right)}{\left(M \text{ x } Q\right)} \text{ x } 100 \qquad (5)$$

Where 'F' denote as Faraday constant, 'C_{NH3}' is concentration of ammonia produced; 'V' is volume of electrolyte, 'M' is the atomic mass of ammonia, 'Q' is net charge went through the electrode during ENRR experiment.

SI 6: Determination of NO_x contaminants

The quantification of NO_x was carried out using spectrophotometric method involving *N*-(-1-naphthyl) - ethylenediamine dihydrochloride. The coloring solution was set up by dissolving 0.5 g of sulfanilic acid* in 90 ml of triple distilled water and 5 ml acetic acid* (Merck Co., Ltd.)*, followed by addition of 5 mg of *N*-(1-naphthyl)-ethylenediamine dihydrochloride^ (Loba Chemie Pvt. Ltd.)^ and compensating the solution to 100 ml. Then, 1 ml electrolyte was mixed with 4 ml of colouring solution. Then after incubating for 15 minutes, then Ultraviolet-visible spectrophotometer was used to monitor the absorption spectrum. The calibration plots (concentration-absorbance curves) were done using sodium nitrite* (Merck Co., Ltd.)* solution with sequential increasing concentrations in 0.1 M HCl.

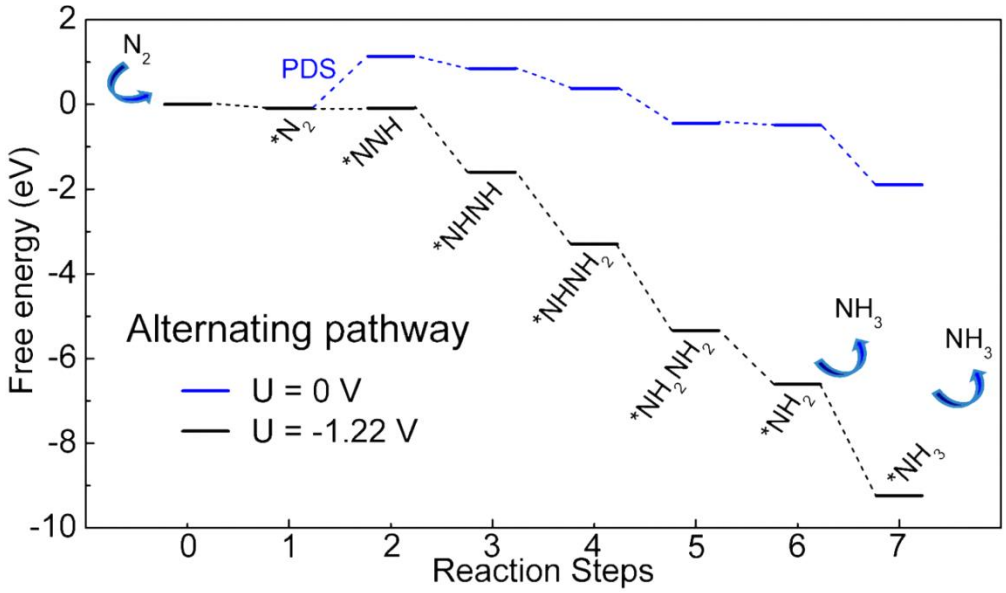

Figure S1: Demonstrate the free energy profile for nitrogen reduction reaction over NiPc considering alternating pathway. Here we consider two applied potential U = 0 V and –1.22 V. Dotted lines are used for guide to eye.

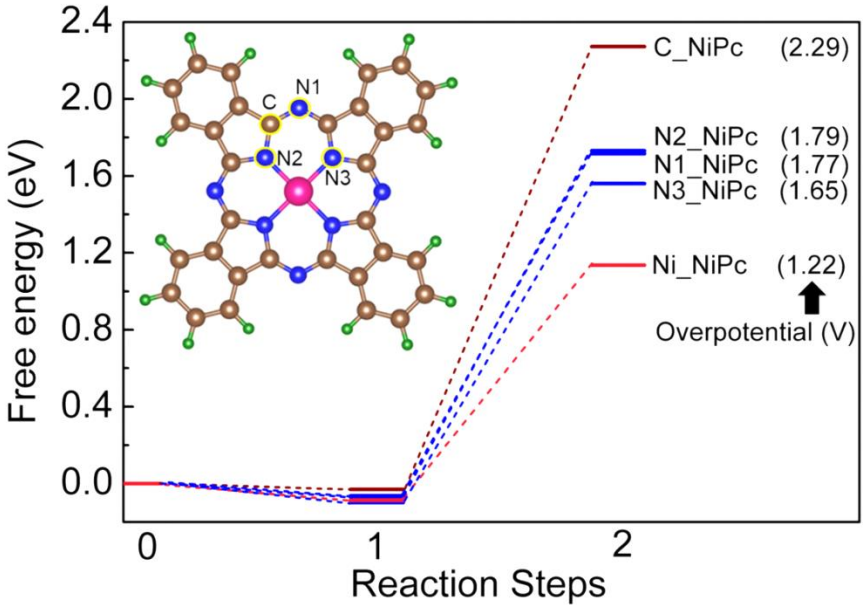

Figure S2 Free energy diagrams for N_2 and NNH adsorption on various sites of NiPc systems.

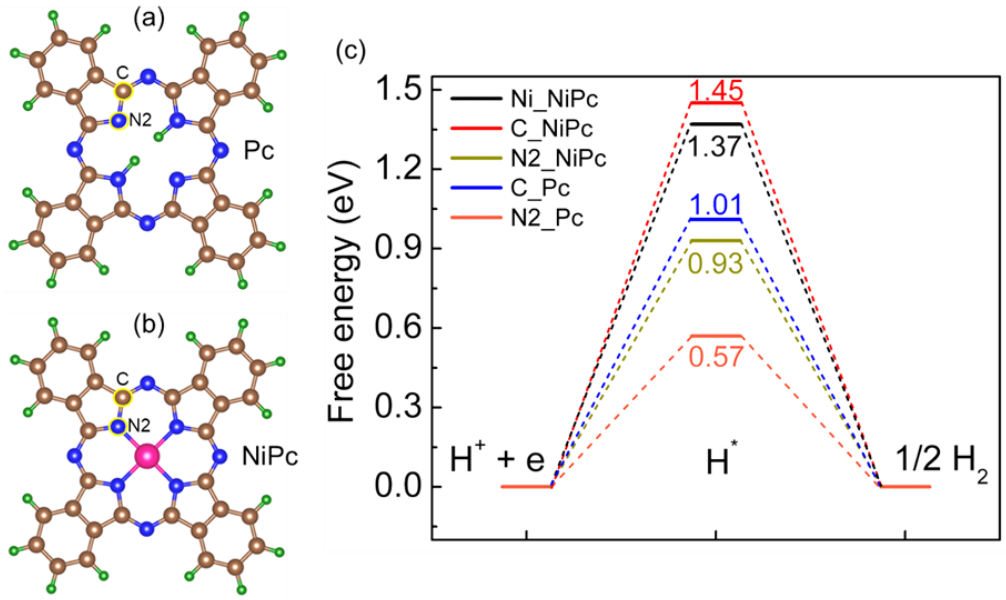

Figure S3: (a) Pc structure with indication of active sites (b) NiPc structure with indication of active sites for HER. (c) Free energy profile of H adsorption during HER on various active sites of Pc and NiPc system.

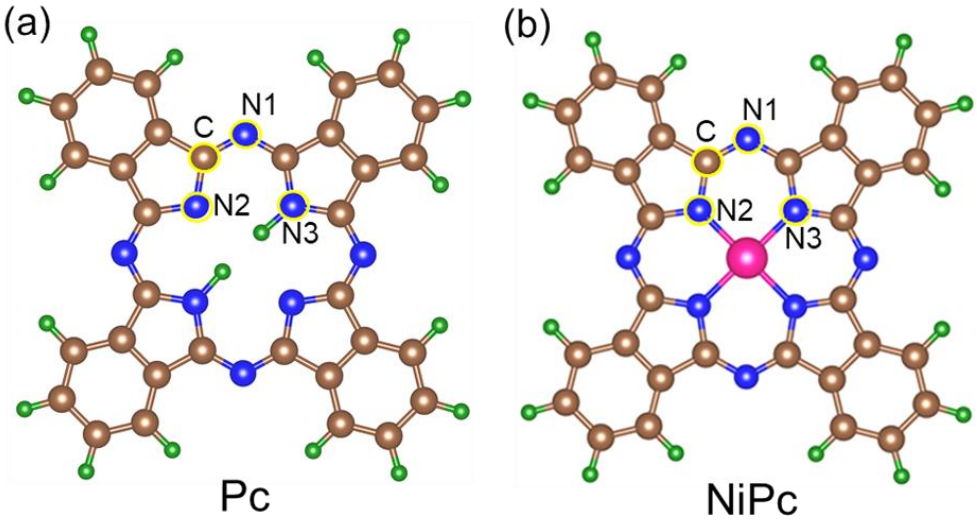

Figure S4: (a) Pc structure with indication of active sites (b) NiPc structure with indication of active sites applied for adsorption of N_2.

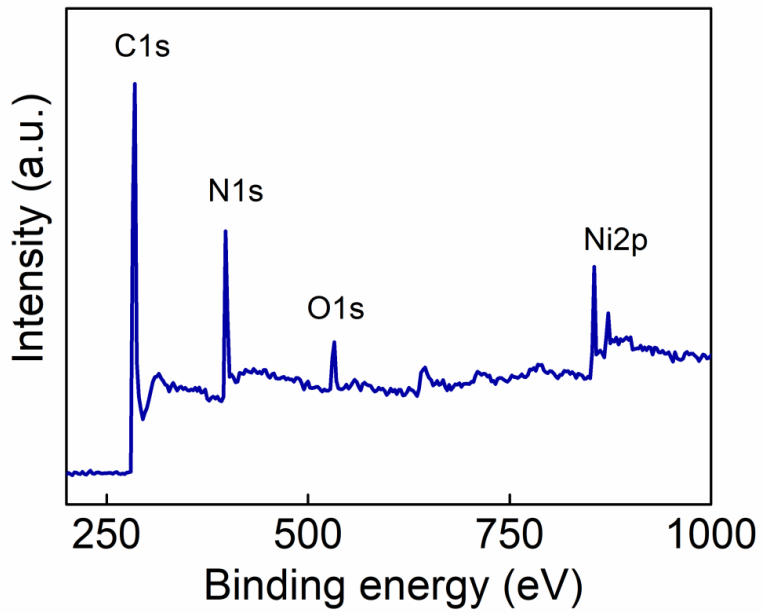

Figure S5: XPS survey scan spectrum of NiPc NRs

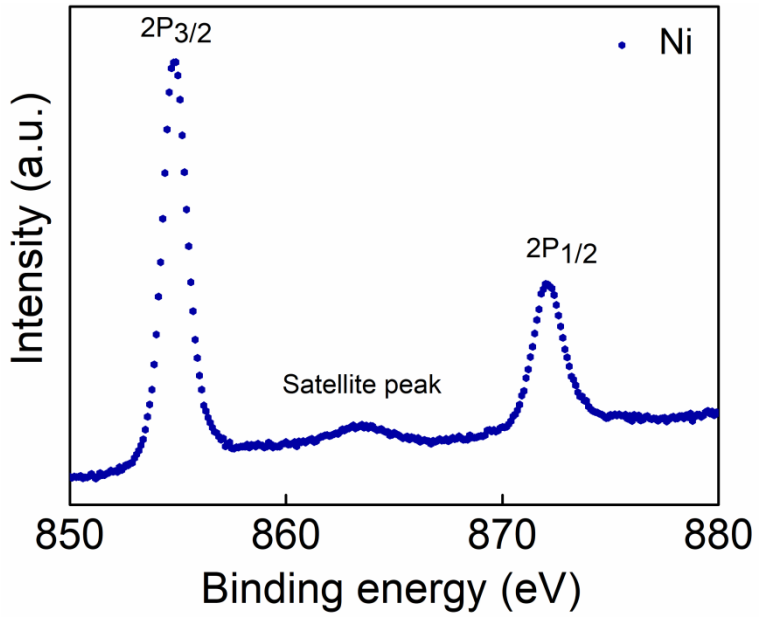

Figure S6: XPS high resolution spectra of Ni 2p doublet

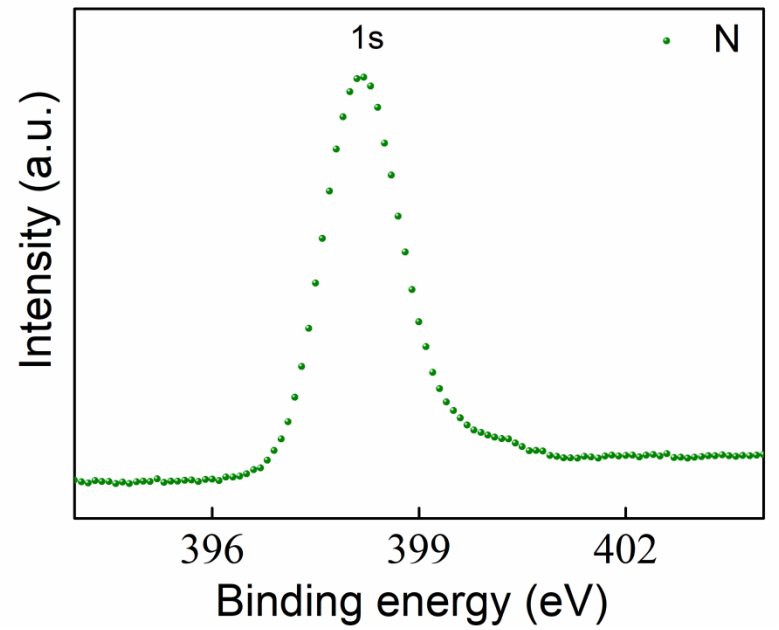

Figure S7: High resolution XPS spectra of N 1s.

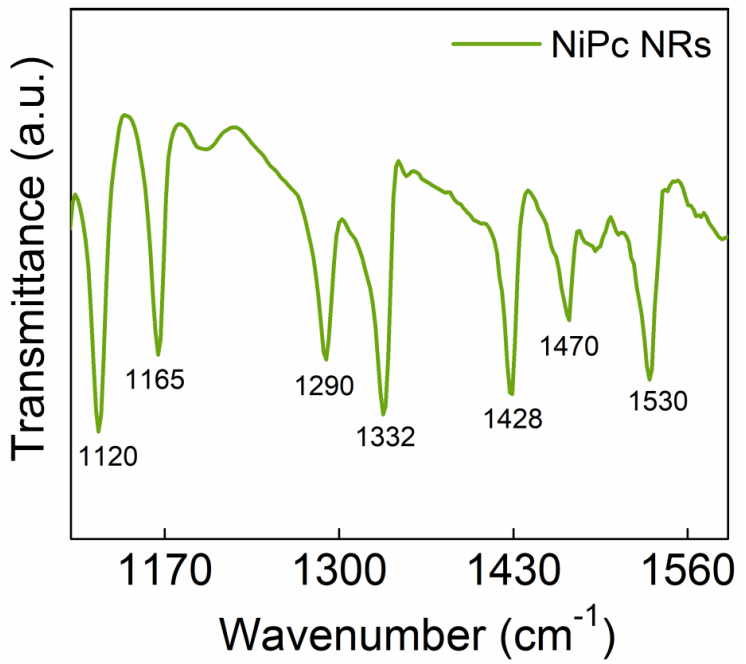

Figure S8: FTIR spectrum of NiPc NRs

The FTIR spectrum of NiPc NRs is shown in the **Figure S8**. From the FTIR spectra, the peak at 1428 cm^{-1} corresponds to the C–C bonds stretching in pyrroles respectively.[6-8] The peak at 1118

cm^{-1} can be assigned to an in-plane bending in benzene ring. [6-8] The peak at 1289 cm^{-1} and 1335 cm^{-1} are related to C=N–C bridge sites.[6-8] The peak at 1165 cm^{-1} can be attributed to Ni–N bonding indicating the formation of NiPc.

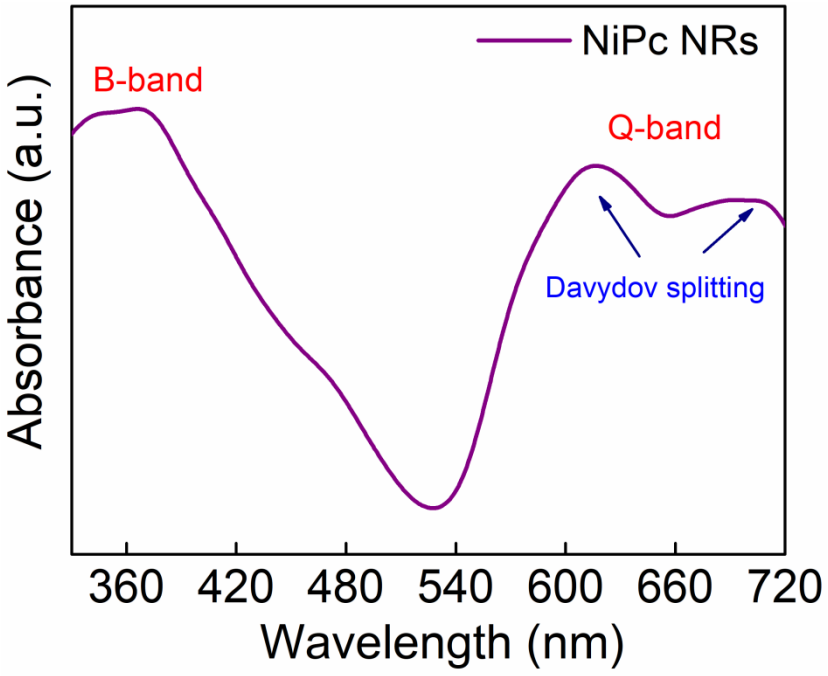

Figure S9: UV-vis spectrum of NiPc NRs

The UV-vis absorptions peaks (**Figure S9**) of NiPc NRs are observed at 368 nm and 615 nm corresponding to the Soret band (B-band) and Q-band respectively.[9] The Soret-band is the strong absorption band in the region of 300 to 500 nm and the Q-band is the weak absorption band in the region of 600 to 750 nm. The Davydov splitting is observed at ~ 616 nm and ~706 nm in the Q-band. [9] The window region of the NiPc nanorod is found at ~527 nm.

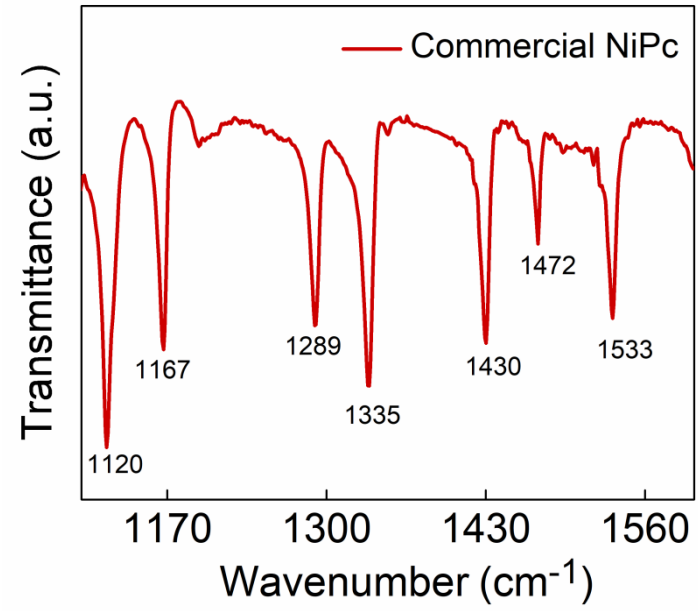

Figure S10: FTIR spectrum of commercial NiPc

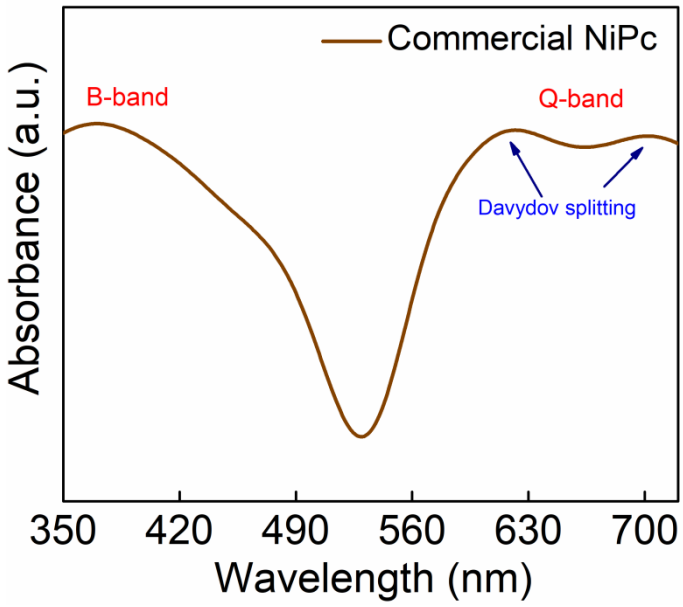

Figure S11: UV-vis spectrum of commercial NiPc

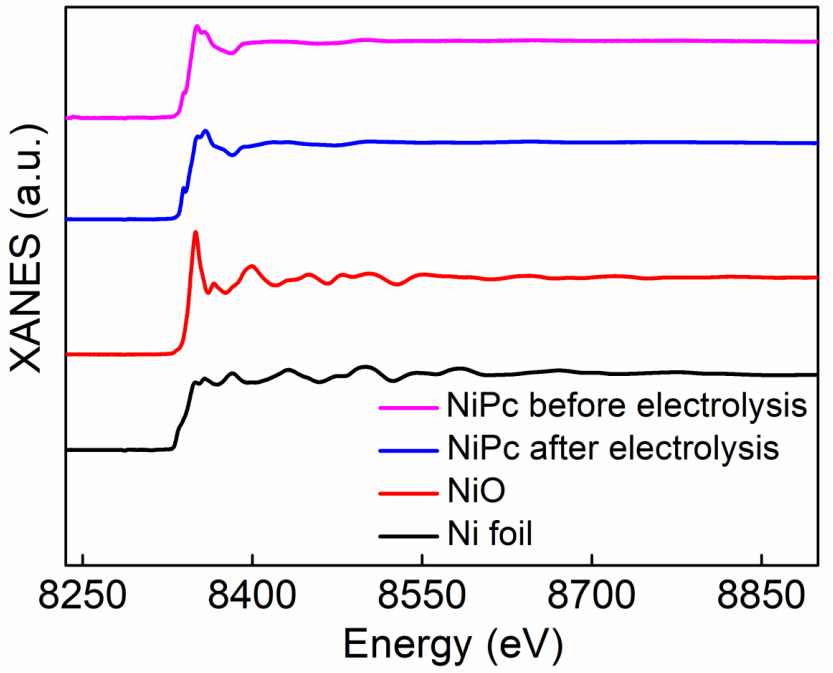

Figure S12: Experimental XANES spectra of NiPc samples measured at Ni K-edge

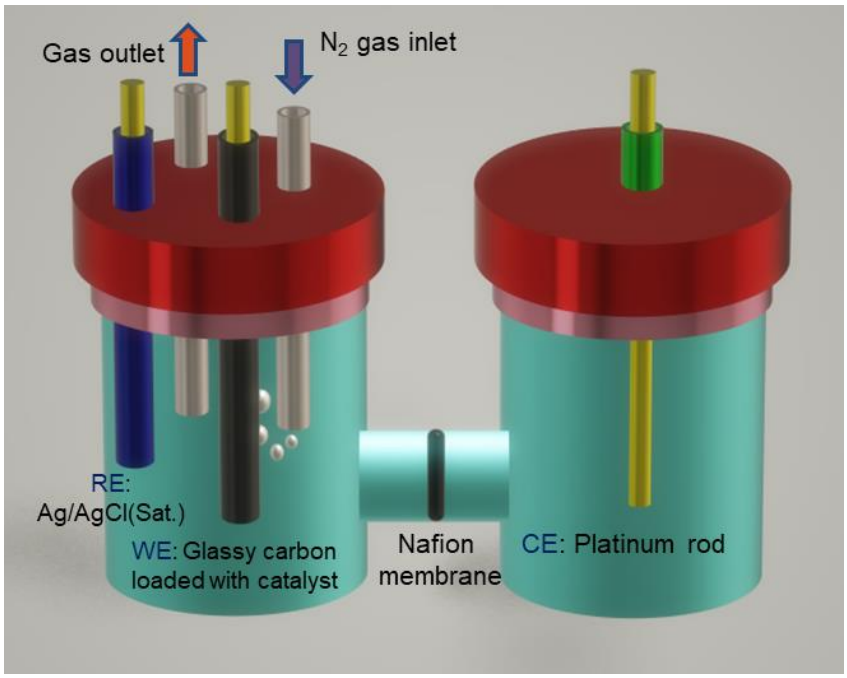

Figure S13: Schematic representation of H-type electrochemical setup

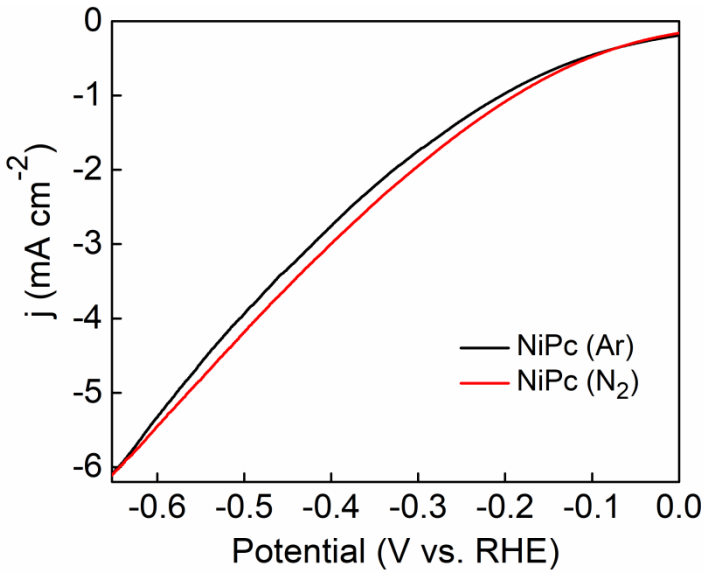

Figure S14: LSV profile of NiPc NRs in Ar & N_2 saturated 0.1 M HCl solution

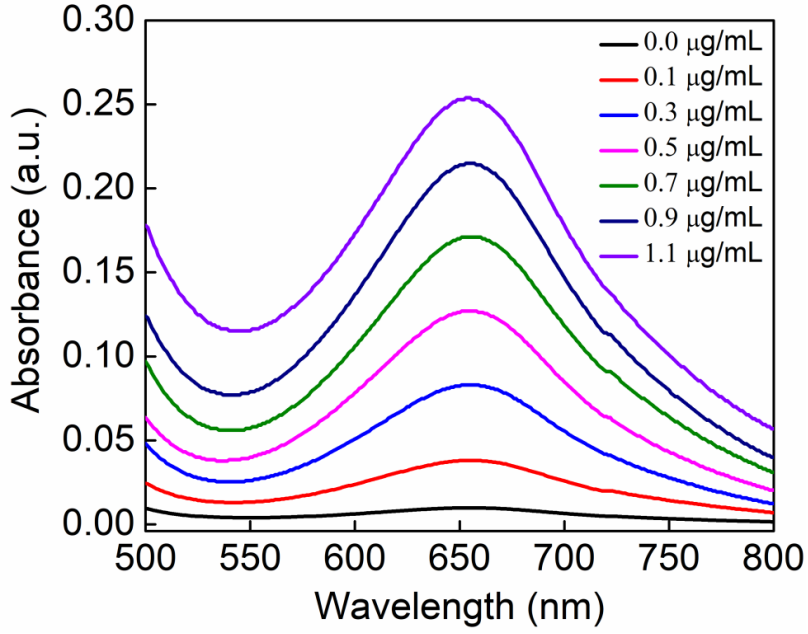

Figure S15: UV-vis spectra of the given concentration of NH_4^+ solution stained with indophenol indicator after 7200 s incubation period.

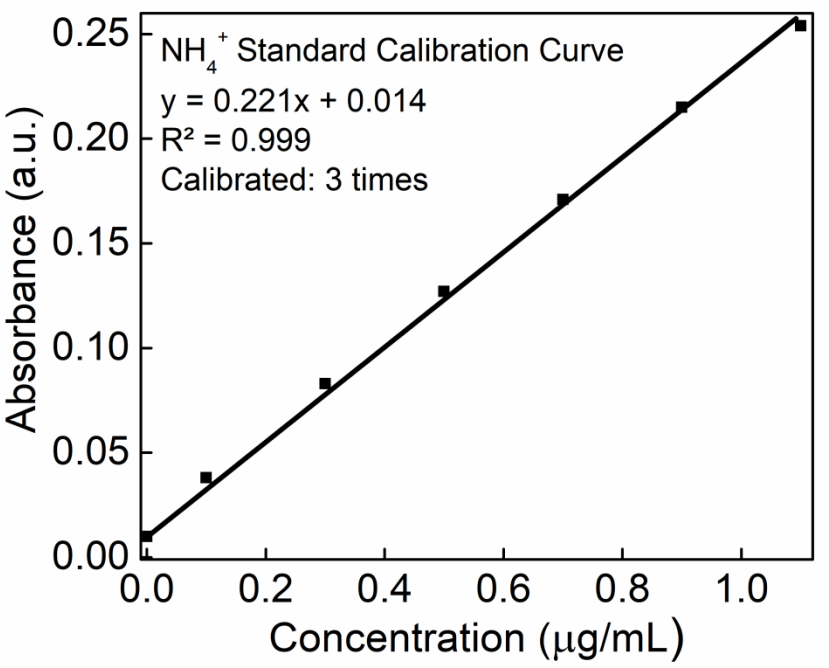

Figure S16: Calibration curve used for calculating the NH_4^+ concentration

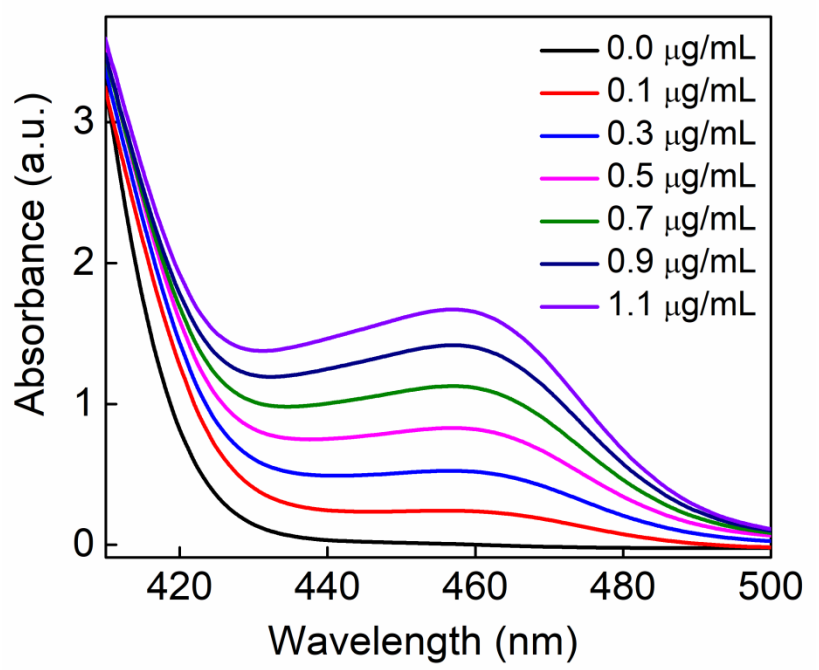

Figure S17 UV-vis absorption spectra of different N_2H_4 concentration after incubated for 600 s under ambient conditions.

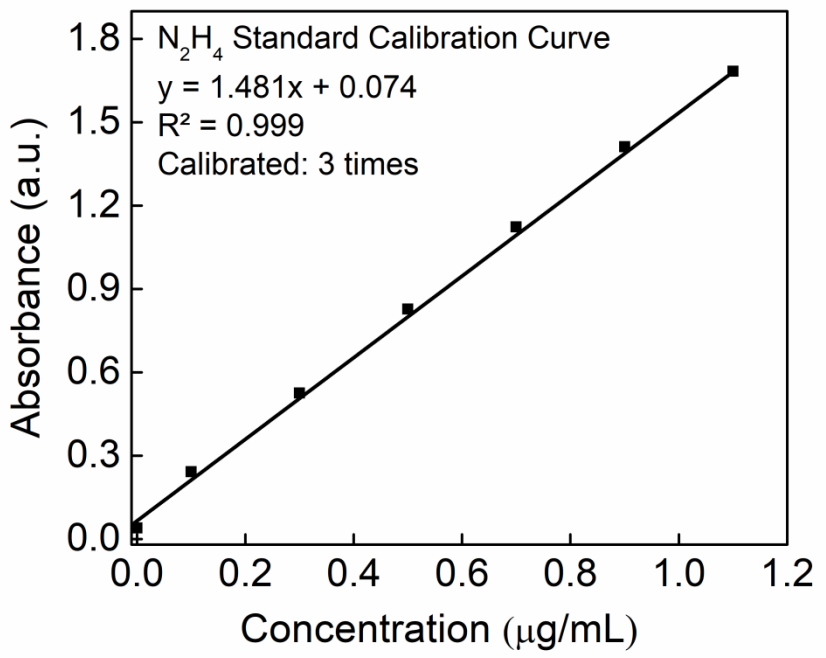

Figure S18: Calibration curve used for determination of N_2H_4 conc.

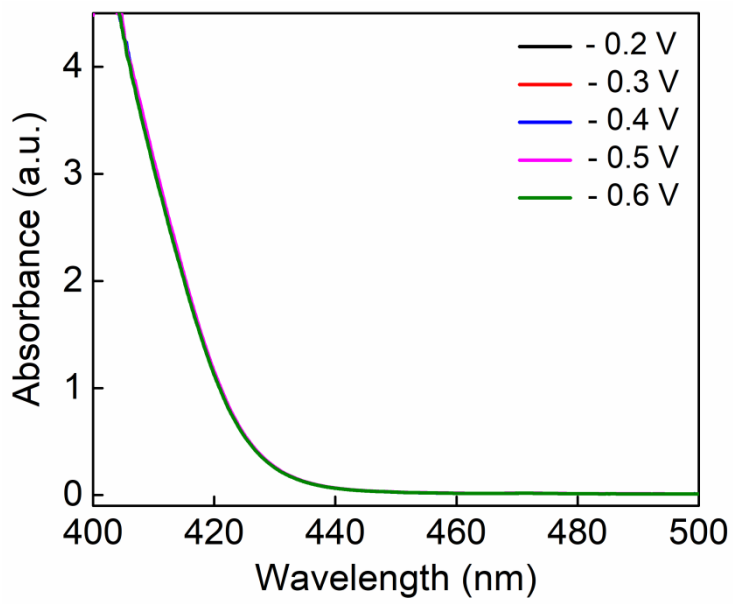

Figure S19: Watt and Chrisp method, UV-vis absorption spectra of electrolytes at different potentials after 6000 s electrolysis of NiPc NRs to quantify formation of hydrazine (if any produced)

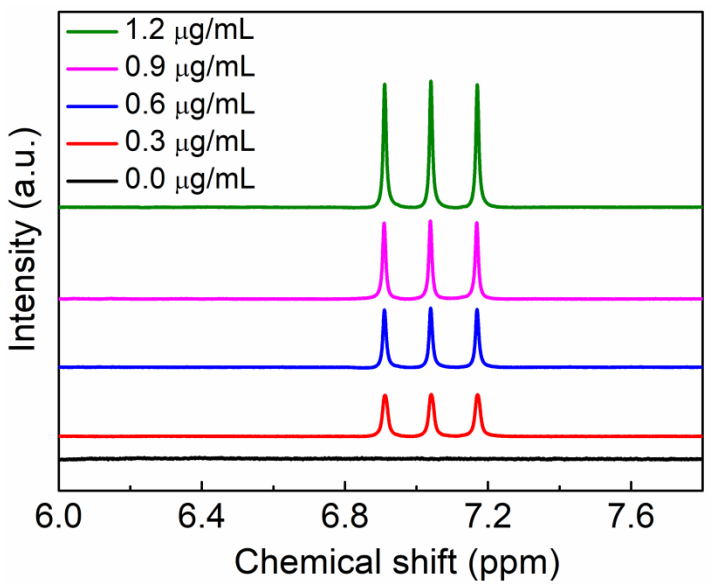

Figure S20: ^{1}H NMR spectra of $(^{14}NH_4)_2SO_4$ with varying concentration

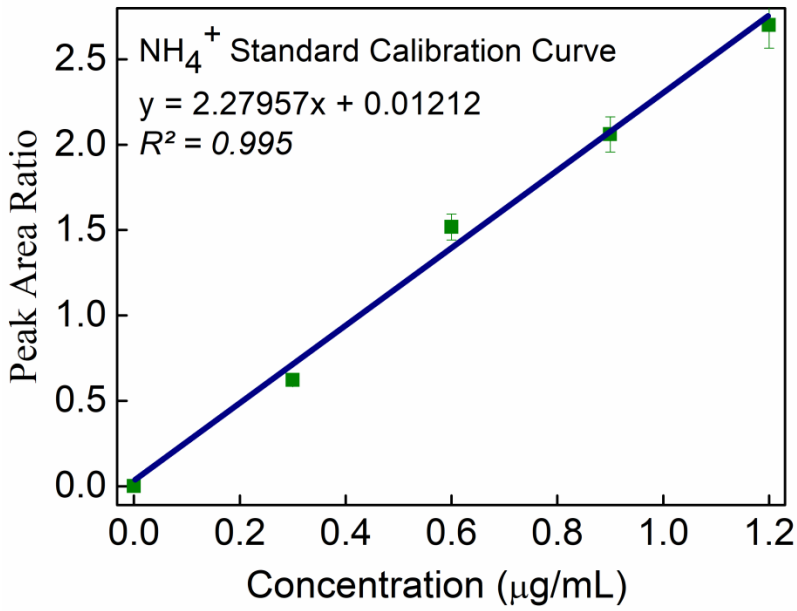

Figure S21: Calibration plot for the determination of $^{14}NH_4^+$ concentration

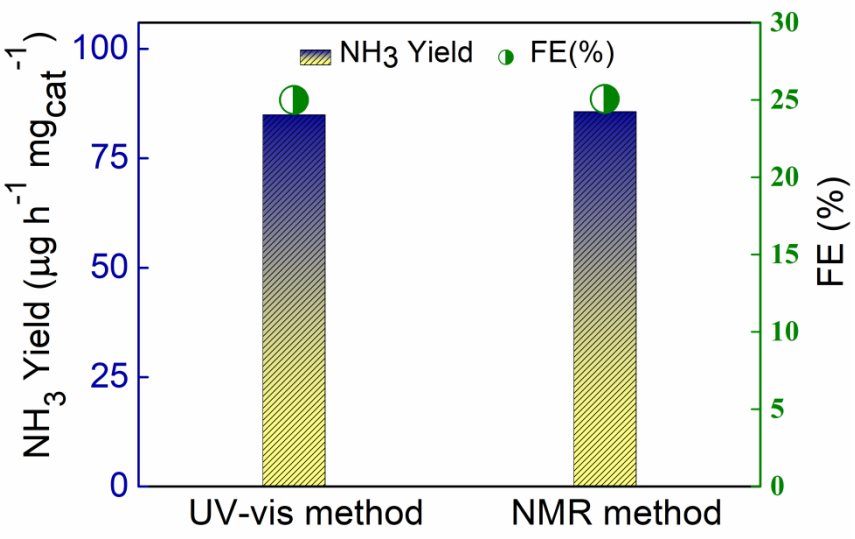

Figure S22: Comparative bar diagram of average NH_3 yield rate by ^1H NMR and UV-vis method

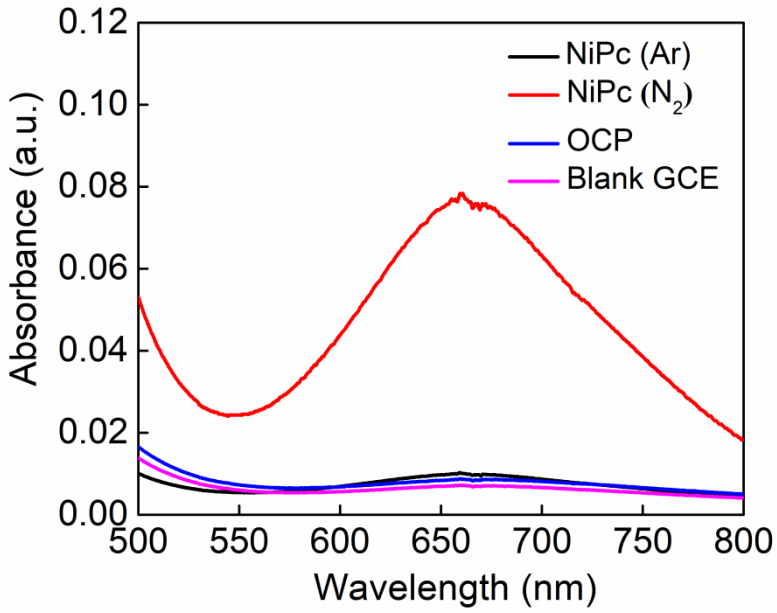

Figure S23: UV-vis absorption spectra of the electrolytes stained with indophenol indicator at –0.3 V *vs.* RHE after 6000 s electrolysis under different conditions (Ar saturated electrolyte at –0.3V *vs.* RHE; N_2 saturated electrolyte at –0.3V *vs.* RHE, open circuit potential and GCE).

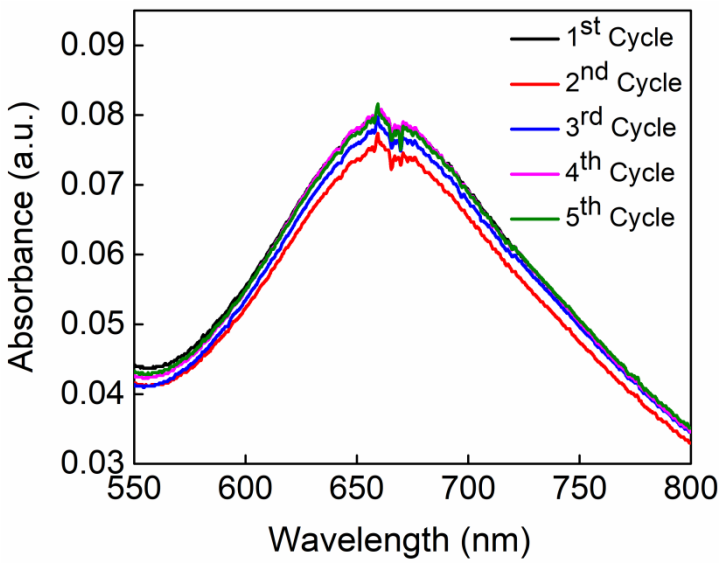

Figure S24: UV-vis absorption spectra of the electrolytes (0.1 M HCl) stained with indophenol indicator at –0.3 V *vs.* RHE after 6000 s electrolysis at a fixed potential (–0.3 V) various cycles.

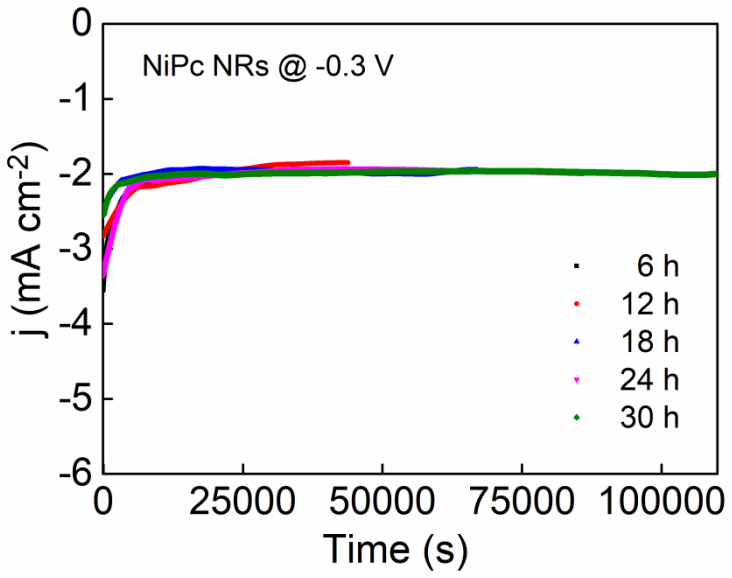

Figure S25: Durability test at different time interval(s) for NiPc NRs towards NRR at –0.3 V *vs.* RHE in N_2 saturated electrolyte.

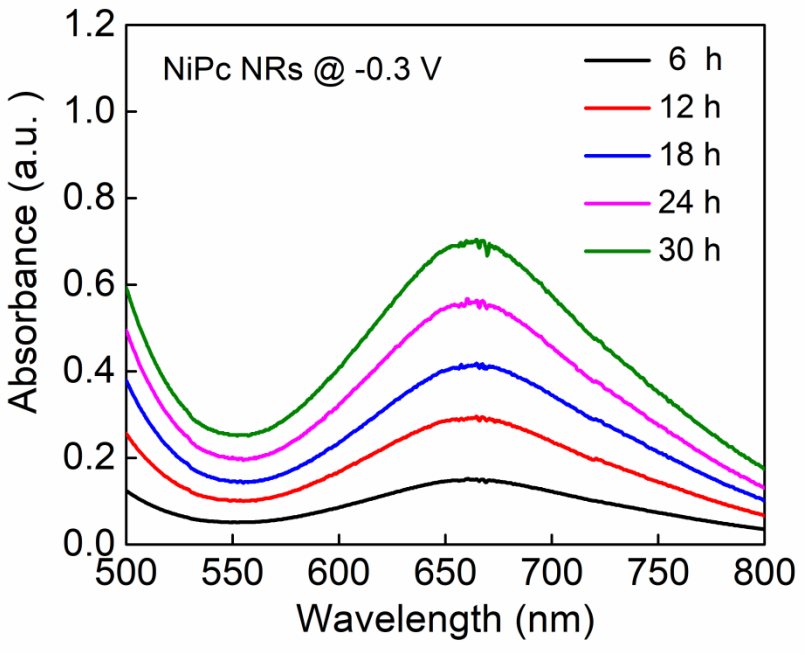

Figure S26: UV-vis absorption of NiPc NRs at –0.3 V *vs.* RHE for long term stability test

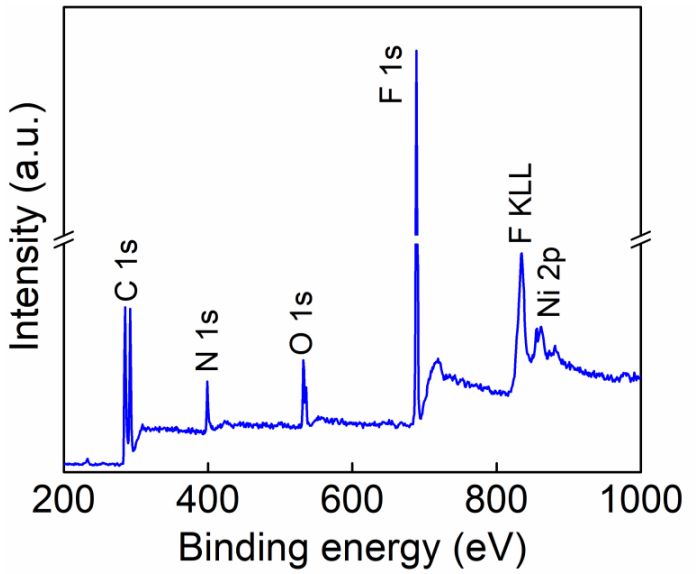

Figure S27: XPS survey scan profile of NiPc NRs after NRR

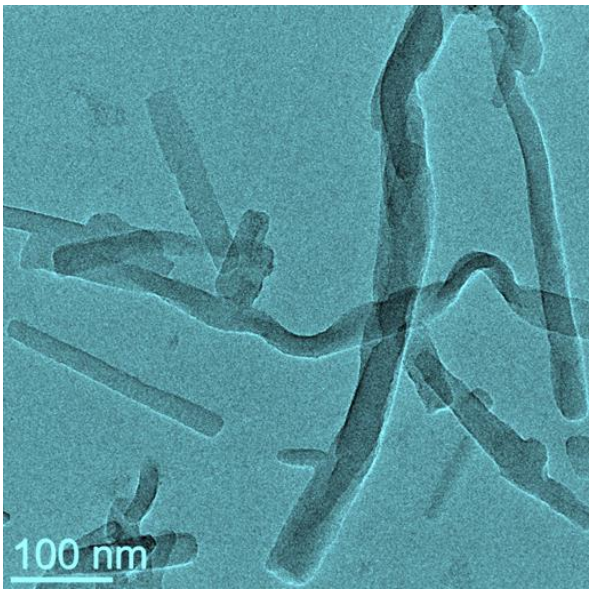

Figure S28: TEM image of NiPc NRs after stability test

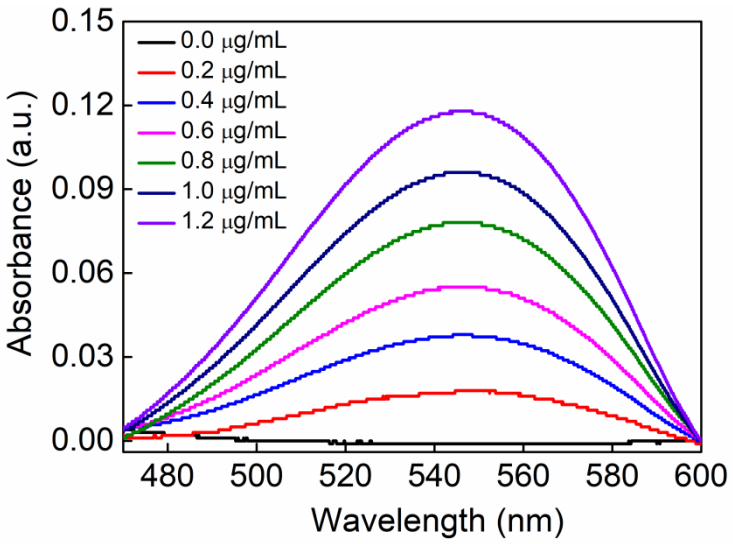

Figure S29: UV-vis absorption spectra of NO_x of various concentration solutions

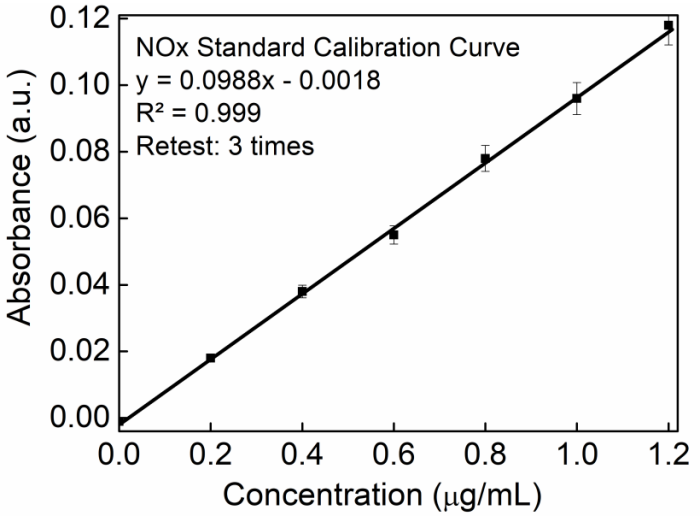

Figure S30: Calibration curve of NO_x with the various concentrations.

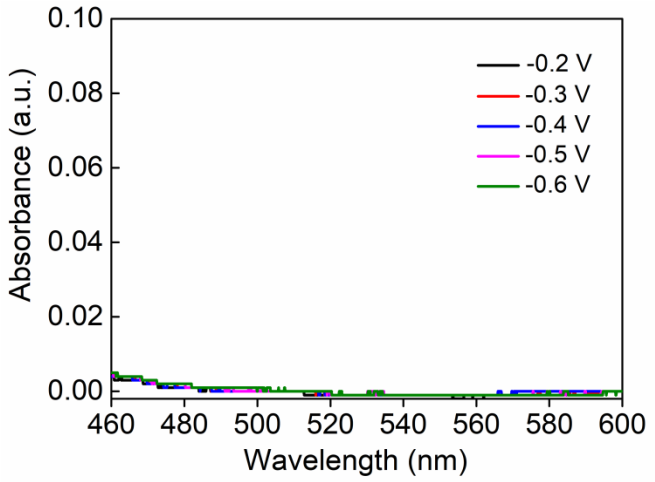

Figure S31: UV-vis spectra of electrolytes saturated with $^{14}N_2$ gas for detecting NO_x.

The absorbance values are very close to zero as compared to the calibration curve, which indicates the absence of NO_x contaminations in the ultra-high purity $^{14}N_2$ feeding gas. Hence it establishes the fact that feeding gas is solely responsible for ammonia production.

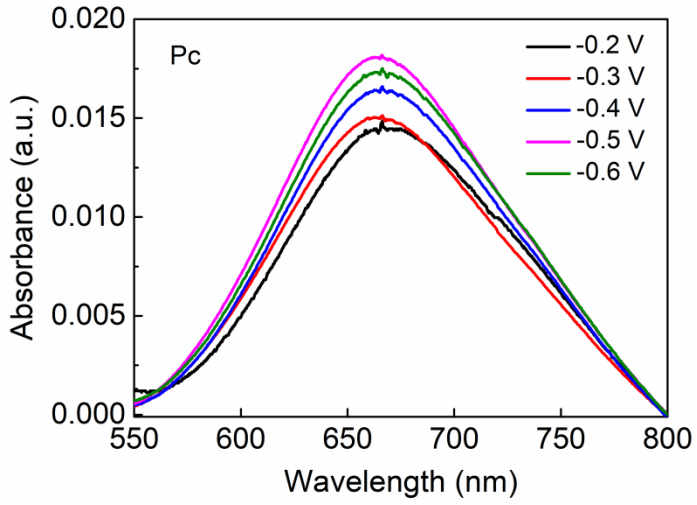

Figure S32: UV-vis absorption spectra of the electrolytes stained with an indophenol indicator at different potential after 6000 s NRR electrolysis

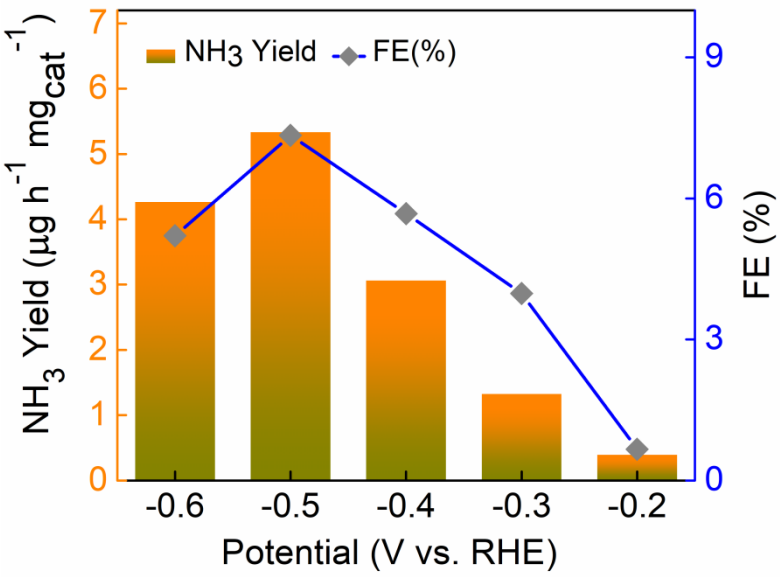

Figure S33: Bar chart of average NH_3 yield rate and corresponding FE of Pc at different potential

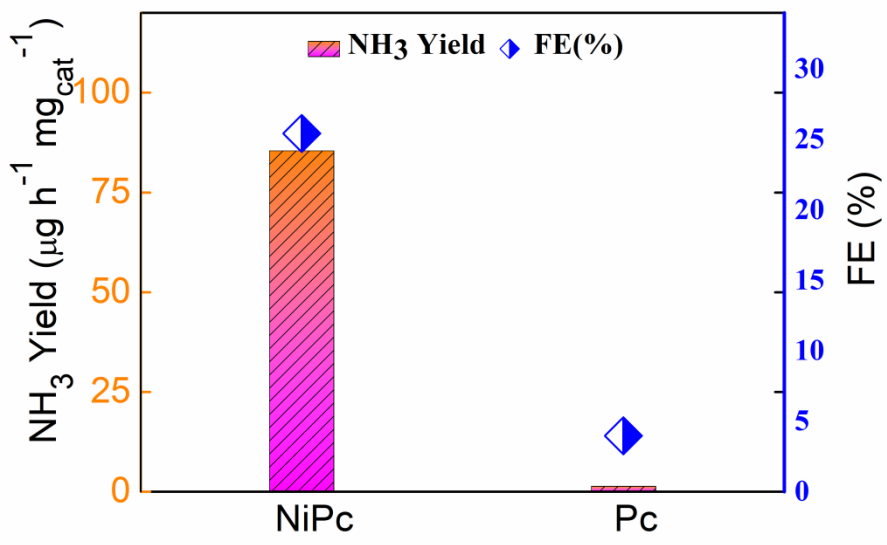

Figure S34: Comparison of NH_3 yield rate and FE of NiPc NRs and Pc at –0.3 V *vs.* RHE

SI 41: Table 1: Comparison of the NRR activity for NiPc NRs with other transition metal based electrocatalyst in solution media of varying pH

Catalyst	**Electrolyte**	**Potential (V *vs.* RHE)**	**NH_3 Yield**	**FE (%)**	**References**
TiO_2 NPs mixed-valent copper	0.5M $LiClO_4$	–0.55 V	21.31 μg h^{-1} mg_{cat}^{-1}	21.99 %	*Adv. Mater.* 2020, **32** (30), 1–8
Cr_2O_3 microsphere	0.1M Na_2SO_4	–0.90 V	25.3 μg h^{-1} mg_{cat}^{-1}	6.78%	*ACS Catal.* 2018, **8**, 9, 8540–8544
PdCu nanoparticles	0.5 M LiCl	–0.1 V	35.7 μg h^{-1} mg_{cat}^{-1}	11.5 %	*Angew. Chemie – Int. Ed.* 2020, **59** (7), 2649–2653

W_2N_3 nanosheet	0.1 M KOH	–0.2 V	11.66 ±0.98 μg h^{-1} mg_{cat}^{-1}	11.67 ± 0.93 %	*Adv. Mater.* 2019, **31** (32), 1–8
Oxygen vacancies on NiO	0.1M Na_2SO_4	–0.5 V	29.1 μg h^{-1} mg_{cat}^{-1}	10.8%	*Inorg. Chem. Front.* 2020, **7**, 455-463
MoSAs-Mo_2C/NCNTs	0.005M H_2SO_4 and 0.1 M K_2SO_4	–0.25V	16.1 μg h^{-1} cm^{-2}_{cat}	7.1%	*Adv. Mater.* 2020, **32** (33), 1–8
Bimetallic Mo-Co nanoparticles	0.1M Na_2SO_4	–0.1V	89.8 μmol h^{-1} g^{-1}_{cat}	13.5%	*J. Mater. Chem. A* 2020, **8**, 9091-9098
NiTe nanocrystals	0.1M HCl	–0.1V	33.34 ± 0.70 μg h^{-1} mg^{-1}	17.38 ± 0.36%	*Adv. Funct. Mater.* 2020, **30** (39), 2004208
CoVP@NiFeV-LDHs	0.05M H_2SO_4	–0.3V	1.6×10^{-6} mol h^{-1} cm^{-2}	13.8%	*Appl. Catal. B Environ.* 2020, **265**, 118559
CoPc nanotubes	0.1 M HCl	–0.3V	107.9 μg h^{-1} mg_{cat}^{-1}	27.7%	*ACS nano* 2021, **15**, 5230-5239
MOF-derived N_2-doped carbon	0.1M KOH	–0.3V	7.3×10^{-6} mol cm^{-2} h^{-1}	10.2%	*Nano Energy* 2018, **48**, 217–226
MoO_2/graphene hybrid	0.1M Na_2SO_4	–0.35V	37.4 μg h^{-1} mg^{-1}	6.6%	*Catal. Sci. Technol.* 2019, **9**, 4248-4254
OVs-$BiVO_4$	0.2 M Na_2SO_4	–0.5V	8.60 μg h^{-1} mg_{cat}^{-1}	10.04%	*Small Methods* 2019, **3** (6), 2–7
Au–Fe_3O_4 NPs	0.1M KOH	–0.2V	21.42 μg h^{-1} mg_{cat}^{-1}	10.54%	*Adv. Funct. Mater.* 2019, **30**, 1906579–1906587
Cr_2O_3- rGO	0.1M KOH	–0.7V	33.3 μg h^{-1} mg_{cat}^{-1}	7.33%	*Inorg. Chem.*

		(yield) –0.6V (FE)			2019, **58**, 2257–2260
FePc grafted on an O-MWCNT	0.1M HCl	–0.3V	36 μg h^{-1} mg_{cat}^{-1}	9.73%	*Chem. Commun*. 2019, **55**, 14111–14114
Fe-doped TiO_2	0.1M $LiClO_4$	–0.4V	25.47 μg h^{-1} mg_{cat}^{-1}	25.6%	*Angew. Chemie - Int. Ed.* 2019, **58**, 18449–18453
Nb_2O_5 nanofiber	0.1M HCl	–0.55V	43.6 μg h^{-1} mg_{cat}^{-1}	9.26%	*Nano Energy* 2018, **52**, 264–270
Mo-MnO_2 NFs	0.1 M Na_2SO_4	–0.5V (yield) –0.4V (FE)	36.6 μg h^{-1} mg_{cat}^{-1}	12.1%	*Appl. Catal. B Environ*. 2020, **264**, 118525
CoO-QD/rGO	0.1 M Na_2SO_4	–0.6V	21.5 μg h^{-1} mg_{cat}^{-1}	8.3%	*J. Mater. Chem. A* 2019**, 7**, 4389-4394
Au/CeOx–rGO	0.1 M HCl	–0.2V	8.3 μg h^{-1} mg_{cat}^{-1}	10.1%	*Adv. Mater*. 2017, **29**, 1–6
Fe/CeO_2	0.5M $LiClO_4$	–0.5V (yield) –0.4V (FE)	26.2 μg h^{-1} mg_{cat}^{-1}	14.7%	*J. Mater. Chem. A* 2020, **8**, 5865–5873
FeN_4	0.1M Na_2SO_4	–0.3V	10.25 μg h^{-1} mg_{cat}^{-1}	10.50%	*ACS Catal*. 2019, **9**, 7311–7317
Atomically dispersed Ni site electrocatalyst	0.5 M $LiClO_4$	–0.8V (yield) –0.6 V (FE)	115 μg cm^{-2} h^{-1}	18.5 ± 3%	*Small Methods*, 2020, **4**, 1–11
NiPc NRs	**0.1 M HCl**	**–0.3 V**	**85.42 μg h^{-1} cm^{-2} or 85 μg h^{-1} mg_{cat}^{-1}**	**25%**	**This Work**

SI 42: References

1. A. K. Poswal, A. Agrawal, A. K. Yadav, C. Nayak, S. Basu, S. R. Kane, C. K. Garg, D. Bhattachryya, S. N. Jha and N. K. Sahoo, *AIP Conf. Proc.*, 2014, **1591**, 649–651.

2. S. Basu, C. Nayak, A. K. Yadav, A. Agrawal, A. K. Poswal, D. Bhattacharyya, S. N. Jha and N. K. Sahoo, *J. Phys. Conf. Ser.*, 2014, **493**, 3–7.

3. X-Ray Absorption: Principles, Applications, Techniques of EXAFS, SEXAFS and XANES, edited by D.C. Konigsberger and R. Prince (Wiley, New York, 1988).

4. M. Newville, B. Ravel, D. Haskel, J. J. Rehr, E. A. Stern and Y. Yacoby, *Phys. B Phys. Condens. Matter*, 1995, **208**–**209**, 154–156.

5. G. W. Watt and J. D. Chrisp, *Anal. Chem.*, 1952, **24**, 2006–2008.

6. X. Wang, W. Wu, H. Ju, T. Zou, Z. Qiao, H. Gong and H. Wang, *Mater. Res. Express*, 2016, **3**, 1–10.

7. H. Kato, S. Takemura, Y. Watanabe, A. Ishii, I. Tsuchida, Y. Akai, T. Sugiyama, T. Hiramatsu, N. Nanba, O. Nishikawa and M. Taniguchi, *J. Vac. Sci. Technol. A Vacuum, Surfaces, Film.*, 2007, **25**, 1147–1151.

8. D. Verma, R. Dash, K. S. Katti, D. L. Schulz and A. N. Caruso, *Spectrochim. Acta - Part A Mol. Biomol. Spectrosc.*, 2008, **70**, 1180–1186.

9. K. P. Madhuri and N. S. John, *Appl. Surf. Sci.*, 2018, **449**, 528–536.